Research Square

Preprints are preliminary reports that have not undergone peer review.
They should not be considered conclusive, used to inform clinical practice,
or referenced by the media as validated information.

Iron modified coal gangue for light assisted attenuation of aqueous hexavalent chromium

Xining Ren

rxning@126.com

China University of Mining and Technology

Junliang Dong

China University of Mining and Technology

Xiaobo Liu

Shenhua XinJie Energy Co., Ltd

Research Article

Keywords: Coal gangue; Iron modification; Hexavalent chromium; Photoreduction; Water treatment; Chromium speciation

Posted Date: November 12th, 2026

DOI: https://doi.org/10.21203/rs.3.rs-11703130/v1

License: This work is licensed under a Creative Commons Attribution 4.0 International License.
Read Full License

Additional Declarations: No competing interests reported.

Iron modified coal gangue for light assisted attenuation of aqueous hexavalent chromium

Xining Ren[1,2*], Junliang Dong[1,2], Xiaobo Liu[2]

1 School of Mines, China University of Mining and Technology, Xuzhou 221116, China

2 Shenhua XinJie Energy Co., Ltd., Ordos 017200, Inner Mongolia, China

* Corresponding author: Xining Ren; email: rxning@126.com

Acknowledgments

This work was supported by the project Comprehensive Evaluation of the Oil-Rich Coal Resource Potential and Utilization Prospects in the Taige Temple Mining Area (No. 6000240419).

Abstract

Coal gangue is a potential mineral precursor for water-treatment materials, but the effect of iron modification on aqueous hexavalent chromium [Cr(VI)] attenuation requires evaluation. This study compares a calcined and acid-washed gangue-derived material (SA) with its iron-modified counterpart (SAF) under white light-emitting diode irradiation. SAF was prepared by treatment with an iron nitrate precursor in N,N-dimethylformamide at 200 °C for 15 h, followed by centrifugation, drying, and calcination in air at 600 °C for 6 h. Powder X-ray diffraction showed similar dominant mineral reflections for SA and SAF, while surface spectroscopy and elemental mapping detected iron in SAF. Relative to SA, SAF exhibited a higher transient photocurrent and a smaller electrochemical impedance arc under the measurement conditions. The concentration profiles indicate faster aqueous Cr(VI) attenuation by SAF at pH 7 than by SA, with a steeper decline for acidified SAF at pH 3. Quantitative rate comparisons require validated sampling and concentration measurements. These observations do not independently establish complete chromium removal, a specific iron oxide phase, or a zeolite heterojunction. A possible contribution from light-driven electron transfer is discussed alongside adsorption and iron-mediated reactions. The findings identify an iron-modified gangue-derived material for further investigation, with chromium mass balance, iron leaching, independent replication, and authentic wastewater testing required to establish environmental applicability.

Keywords: Coal gangue; Iron modification; Hexavalent chromium; Photoreduction; Water treatment; Chromium speciation

1 Introduction

Hexavalent chromium [Cr(VI)] is a water-pollution concern because its mobility and biological effects differ substantially from those of trivalent chromium [Cr(III)] (Ge et al., 2021; Islam et al., 2025). Chromium speciation depends on pH, redox conditions, concentration, and interactions with mineral surfaces. Acidification can dissolve Cr(III) hydroxide, but dissolution does not itself convert Cr(III) to Cr(VI). Reduction of Cr(VI) and subsequent management of Cr(III) are therefore distinct treatment steps (Fendorf, 1995; Djellabi et al., 2022).

Conventional chromium-treatment approaches include chemical reduction, adsorption, ion exchange, and membrane separation (D. Wang et al., 2025; Xu et al., 2025). Their suitability depends on the wastewater matrix (Sutrisna et al., 2022), reagent demand, residual chromium concentration, and management of spent solids. Photocatalytic reduction provides a route for transferring reducing equivalents to Cr(VI) (D. Liu et al., 2023; W. Liu et al., 2022; Rajappa et al., 2024; X.-Z. Sun et al., 2023; Zheng et al., 2024), but performance depends on light delivery, electron donors, surface chemistry, and the fate of the reduction products (Zhao et al., 2019; Y. Sun et al., 2023). A decrease in the concentration of dissolved Cr(VI) alone cannot establish removal of total chromium from water.

Research on water treatment also addresses analytical selectivity through fluorescent Cr(VI) probes (Lv et al., 2023) and operational stability through investigations of membrane fouling associated with sludge bulking (Wu et al., 2023). Related studies of photocatalyst design examine S-scheme junctions incorporating quantum dots (S. Li et al., 2025; Zhu et al., 2025), catalysts supported on molecular sieves for degradation of organic pollutants (Nizam et al., 2022; R.-Q. Wang et al., 2023), and surface or defect modification of titania for photocatalytic hydrogen evolution (Gupta et al., 2023; H. Liu et al., 2025).

Coal gangue has been investigated as a precursor for adsorbents and reactive materials because of its mineral content and availability as a mining residue (Bian et al., 2020; Yang et al., 2025). Its use for chromium treatment is already established. Li and Wang (2018) reported Cr(VI) reduction by coal gangue, and Zhao et al. (2020) investigated gangue-mediated photocatalytic treatment in the presence of tartaric acid. A related study also examined a gangue-derived support combined with UiO-66-NH_2 (Ren et al., 2026). These precedents make the effect of iron modification, rather than the general use of gangue for chromium treatment, the question addressed here.

This study compares a calcined and acid-washed coal-gangue-derived material, denoted SA, with an iron-modified material, denoted SAF. The comparison combines mineral and surface characterization, photoelectrochemical measurements, aqueous Cr(VI) concentration profiles, additive tests, and repeated reaction cycles. The objective is to evaluate whether iron modification is

associated with faster Cr(VI) attenuation and to examine the evidence for possible electron-transfer pathways. The experiments use potassium dichromate solutions; extrapolation to coal-mine water requires testing with representative water chemistry and authentic samples (Baruah & Singh, 2024).

2 Materials and methods

2.1 Reagents and material nomenclature

Potassium dichromate ($K_2Cr_2O_7$), sulfuric acid (H_2SO_4), nitric acid (HNO_3), benzoquinone (BQ), 2,2,6,6-tetramethylpiperidin-1-oxyl (TEMPO, 98%), and 5,5-dimethyl-1-pyrroline N-oxide (DMPO, 98%) were obtained from Beijing InnoChem Science & Technology Co., Ltd. Iron(III) nitrate nonahydrate [$Fe(NO_3)_3·9H_2O$] was used as the iron precursor, and N,N-dimethylformamide (DMF) was used in the reported modification procedure. Isopropanol (IPA) was used in additive experiments. Deionized water was used for aqueous solution preparation and washing.

SA denotes the coal-gangue-derived solid obtained after calcination and acid washing. SAF denotes the iron-modified derivative. These labels identify the preparation history and do not assign a specific zeolite framework or iron oxide crystal phase.

2.2 Preparation of SA and SAF

Coal gangue powder (1 g) was placed in a porcelain boat and calcined in a muffle furnace at 800 °C for 6 h. After cooling, the solid was washed with nitric acid and rinsed with deionized water at least three times. The resulting material was denoted SA, with a recovered mass yield of 70%.

For iron modification, SA (1 g), $Fe(NO_3)_3·9H_2O$ (0.1 mmol), and DMF (50 mL) were placed in a 100 mL autoclave. The sealed vessel was heated at 200 °C for 15 h for solvothermal treatment. The solid was recovered by centrifugation and dried. The dried solid was then calcined in air at 600 °C for 6 h to obtain SAF.

2.3 Characterization

Powder X-ray diffraction (PXRD) was performed using a Bruker D8 Advance diffractometer. X-ray photoelectron spectroscopy (XPS) was performed using a Thermo ESCALAB 250XI instrument.

Transmission electron microscopy (TEM) and high-resolution TEM were performed using a JEOL JEM-3000F microscope at an accelerating voltage of 200 kV. Elemental maps were used to examine the spatial distribution of the detected elements. Ultraviolet–visible diffuse reflectance spectra were recorded using a Varian Cary 500 spectrophotometer.

Photoelectrochemical measurements were conducted using a Metrohm-Autolab AUT302N workstation. The three-electrode arrangement used Ag/AgCl as the reference electrode and a coiled platinum wire as the counter electrode. Transient photocurrent and electrochemical impedance measurements were used to compare SA and SAF. Electron paramagnetic resonance (EPR) spectra were recorded at room temperature using a Bruker A300 X-band instrument; DMPO was used as a spin-trapping reagent.

2.4 Batch experiments and chromium analysis

Batch experiments were conducted in a 300 mL quartz reactor containing 100 mL of an aqueous Cr(VI) solution prepared from $K_2Cr_2O_7$ and 20 mg of SA or SAF. The initial $K_2Cr_2O_7$ concentration was 2 mg L^{-1}, corresponding to approximately 0.707 mg Cr L^{-1}. The initial pH was 7 for the standard SA and SAF experiments and 3 for the acidified SAF experiment, denoted SAF–H^+. The suspension was stirred in the dark for 20 min before irradiation with a 30 W white light-emitting diode (LED) lamp. This dark-contact period was used to distinguish pre-irradiation uptake from subsequent concentration changes.

Suspension aliquots (2 mL) were withdrawn at 20 min intervals during the reaction and filtered before analysis. Cr(VI) was determined by the diphenylcarbazide colorimetric method using a Laspec Alpha-1860 spectrophotometer. Total chromium was measured using a PinAAcle 900T flame atomic absorption spectrometer. Where both measurements refer to the same filtrate and use the same chromium mass basis, dissolved Cr(III) can be estimated as the difference between total dissolved chromium and dissolved Cr(VI). This difference does not quantify chromium retained on the solid.

Chromium concentrations determined by the two analytical methods must be expressed on the same elemental chromium basis when calculating dissolved Cr(III).

The concentration profiles are described as aqueous Cr(VI) attenuation. In Fig. 7a, the plotted normalization uses the concentration before the dark-contact period as the reference. A kinetic analysis of the illuminated period should instead use the Cr(VI) concentration at the onset of irradiation as its reference and should exclude values below the analytical quantification limit.

Additive experiments examined the effects of TEMPO, BQ, and IPA using 20 mg of SAF per experiment. The additive quantity was 0.1 mmol per experiment, with a 30 min irradiation period under the 30 W white LED lamp in air at room temperature. The outcomes are provided in Table S1. Repeated-use experiments comprised five reaction cycles under white LED irradiation, followed by PXRD characterization of recovered solids.

3 Results and discussion

3.1 Mineral structure and iron distribution

SA and SAF show broadly similar PXRD patterns (Fig. 1). The dominant reflections near $2\theta = 20.9°$ and 26.7° are consistent with a quartz-containing mineral matrix. The patterns do not show a separately resolved iron-containing crystalline phase. A weak or absent reflection may reflect a small phase fraction, limited crystallinity, or overlap with the support; it cannot by itself identify the iron species. The available PXRD data also do not establish a particular zeolite framework.

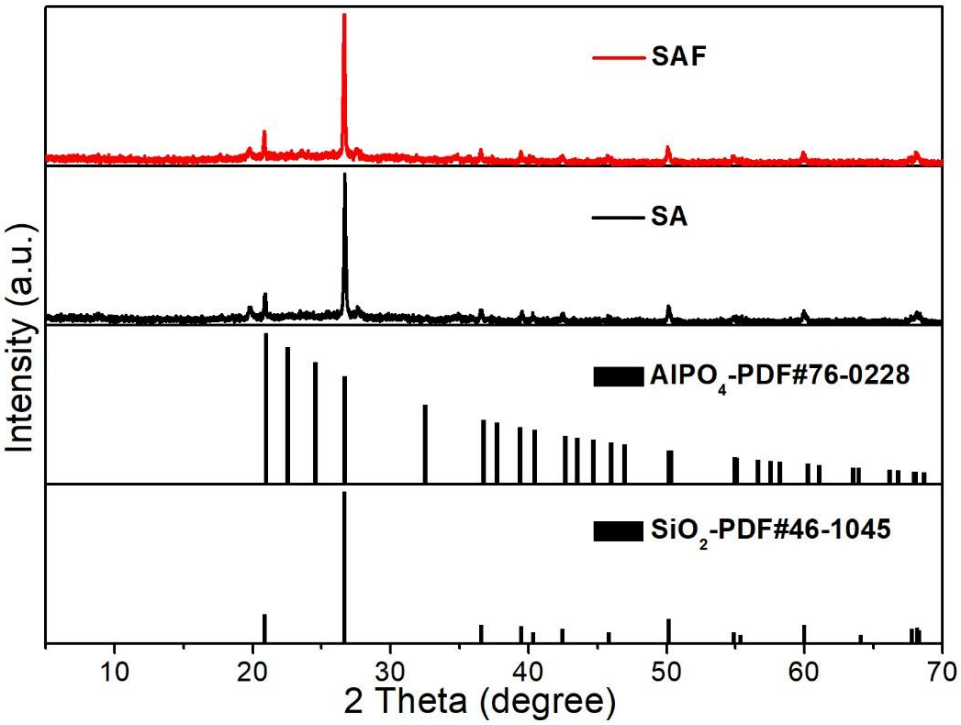


Fig. 1 PXRD patterns of SA and SAF with the displayed SiO_2 and $AlPO_4$ reference patterns

The XPS spectra show Al, Si, and O signals for the gangue-derived materials and an Fe signal for SAF (Fig. 2). Differences in the core-level envelopes are consistent with changes in the surface environment after modification. However, small binding-energy differences require consistent charge correction and fitting before they can be interpreted as interfacial charge transfer. In the Fe 2p region, the lower-binding-energy group corresponds to Fe 2p3/2 and the higher-binding-energy group to Fe 2p1/2; multiplet splitting and satellite features complicate oxidation-state assignment (Biesinger et al., 2011). The spectra are therefore used as evidence for surface iron rather than definitive proof of an exclusively Fe(III) oxide phase.

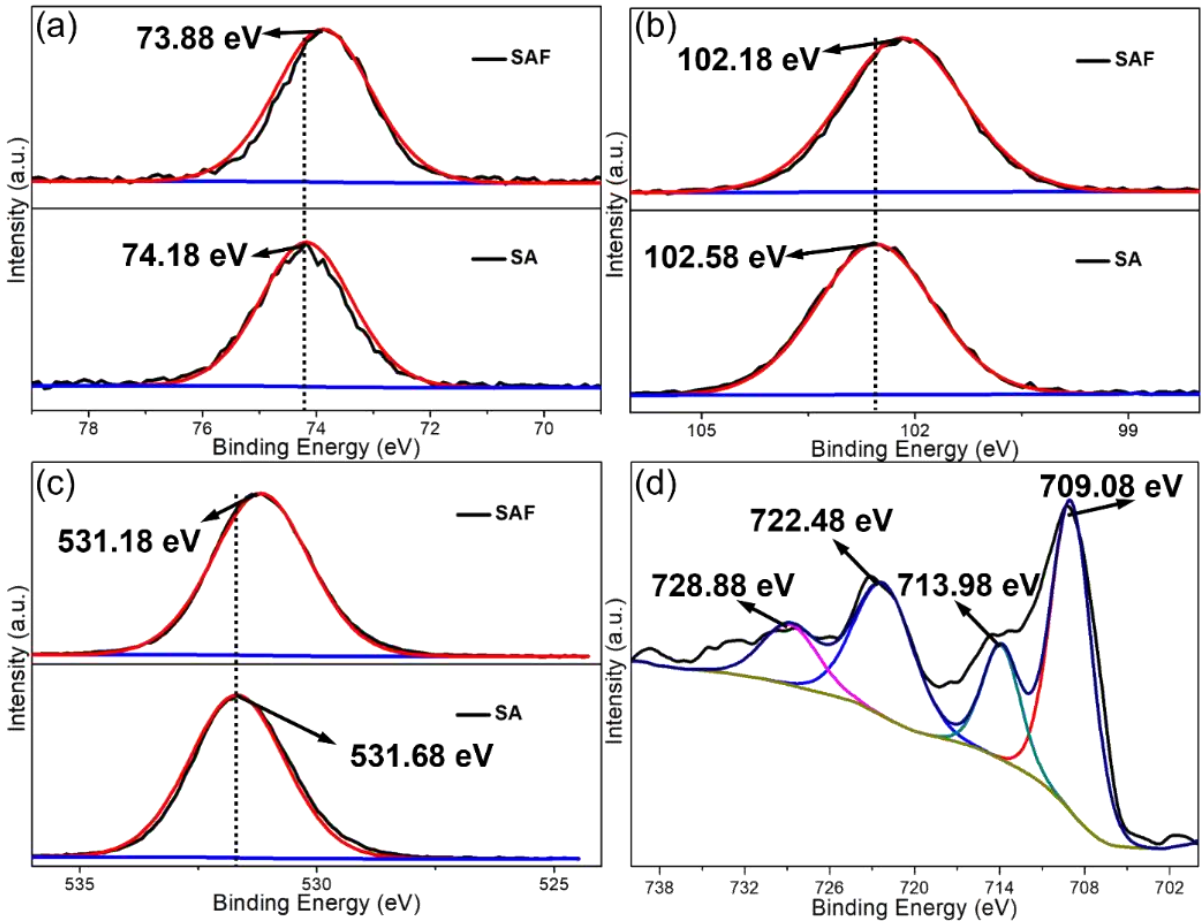


Fig. 2 XPS spectra of SA and SAF in the Al 2p (upper left), Si 2p (upper right), O 1s (lower left), and Fe 2p (lower right) regions

TEM images show irregular particles and aggregates for SA and SAF (Fig. 3). The images do not establish a unique cubic iron-containing structure or permit a quantitative assignment of pore size. Elemental maps of SA show Si, Al, and O (Fig. 4); corresponding maps of SAF additionally show Fe over the mapped region (Fig. 5). These observations support iron incorporation or deposition at the particle scale, without distinguishing framework substitution from surface-bound species. Additional SA elemental maps are provided in Fig. S1.

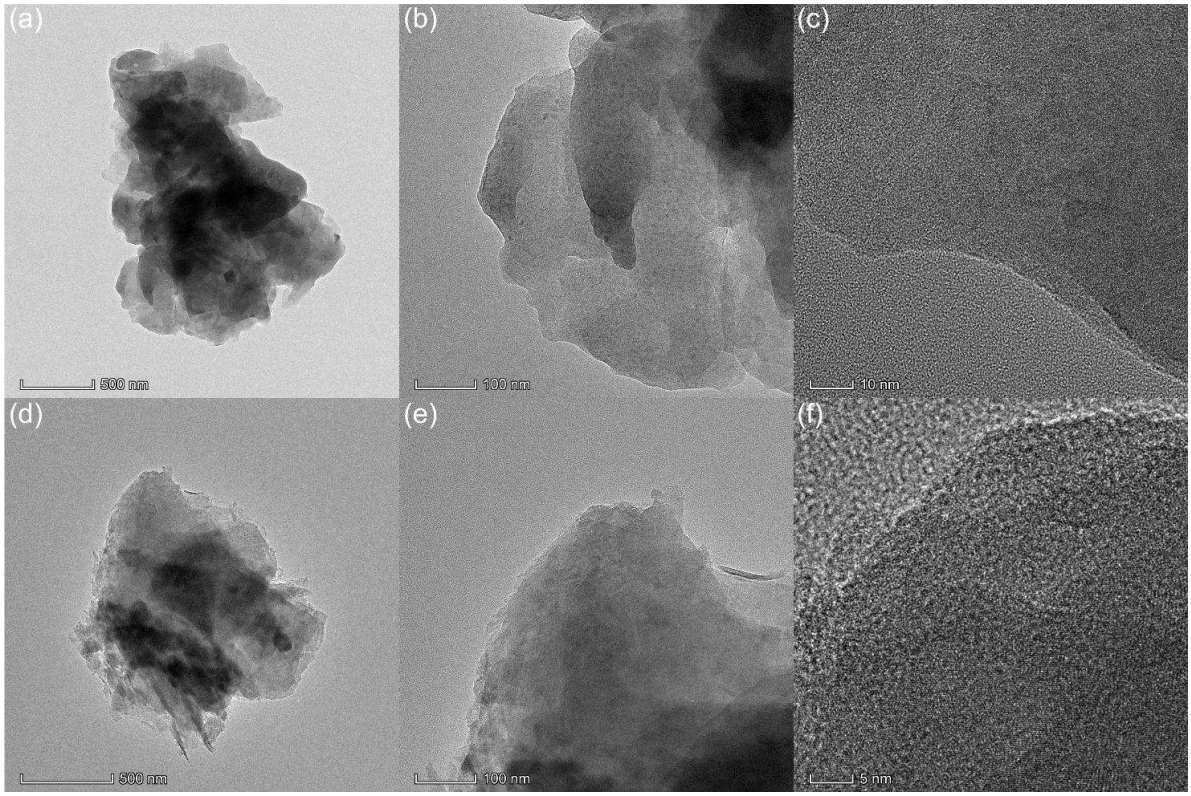


Fig. 3 TEM images of SA (a–c) and SAF (d–f), with scale bars as shown

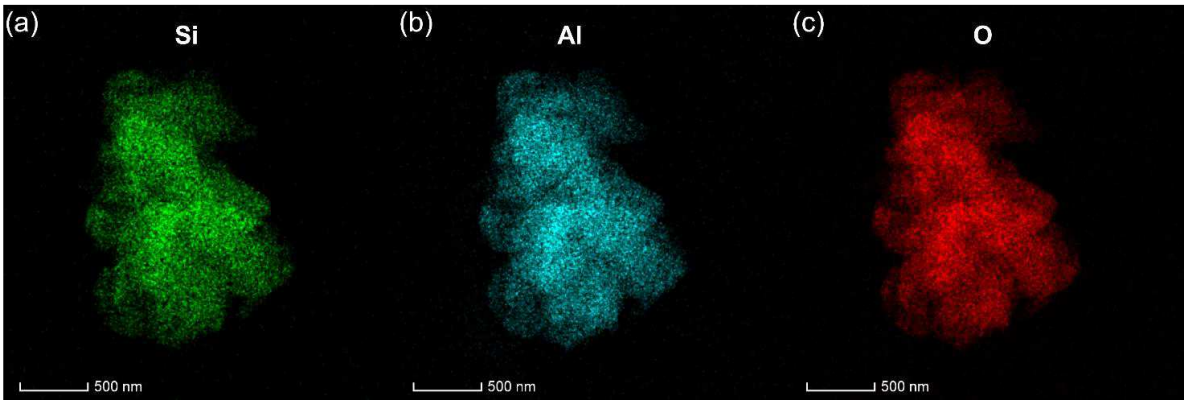


Fig. 4 Elemental maps of SA showing (a) Si, (b) Al, and (c) O

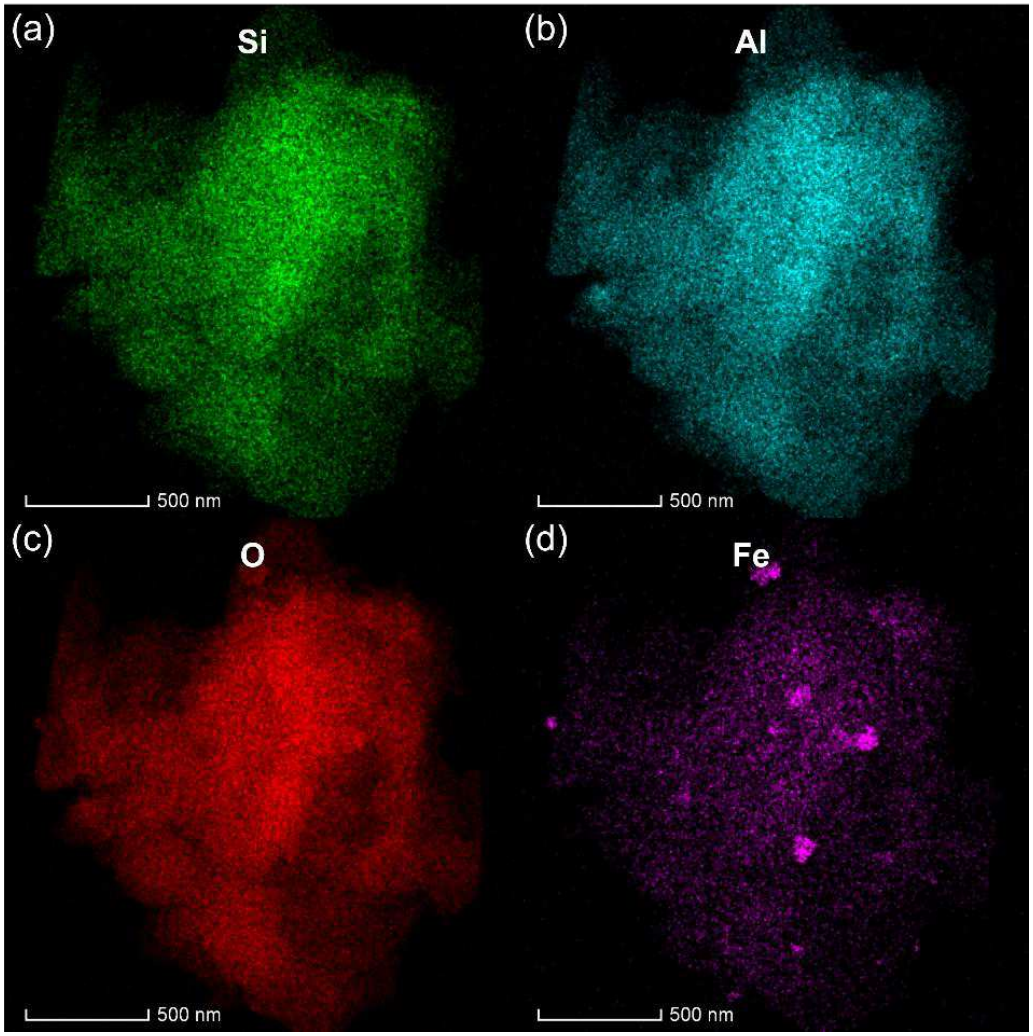


Fig. 5 Elemental maps of SAF showing (a) Si, (b) Al, (c) O, and (d) Fe

3.2 Optical and photoelectrochemical response

The diffuse reflectance spectra show a modest difference between SA and SAF in the visible wavelength region (Fig. 6a). This observation suggests that iron modification affects the optical response, although it does not provide a quantitative band gap or establish a shifted absorption edge. SAF exhibits a larger transient photocurrent than SA under the measurement conditions (Fig. 6b). Its impedance arc is also smaller (Fig. 6c), consistent with a change in the electrode response that may include more favorable charge transfer. Photocurrent depends on film preparation and operating conditions, and an impedance arc alone is not a direct measurement of charge-carrier separation efficiency.

The DMPO-assisted EPR measurement gives a stronger signal for SAF than for SA or the blank (Fig. 6d). This supports the generation of spin-trapped species under the measurement conditions.

Assignment specifically to superoxide requires the trapping medium, control spectra, and hyperfine parameters. Even with that assignment, the presence of a radical does not establish that it is the dominant Cr(VI)-reducing species.

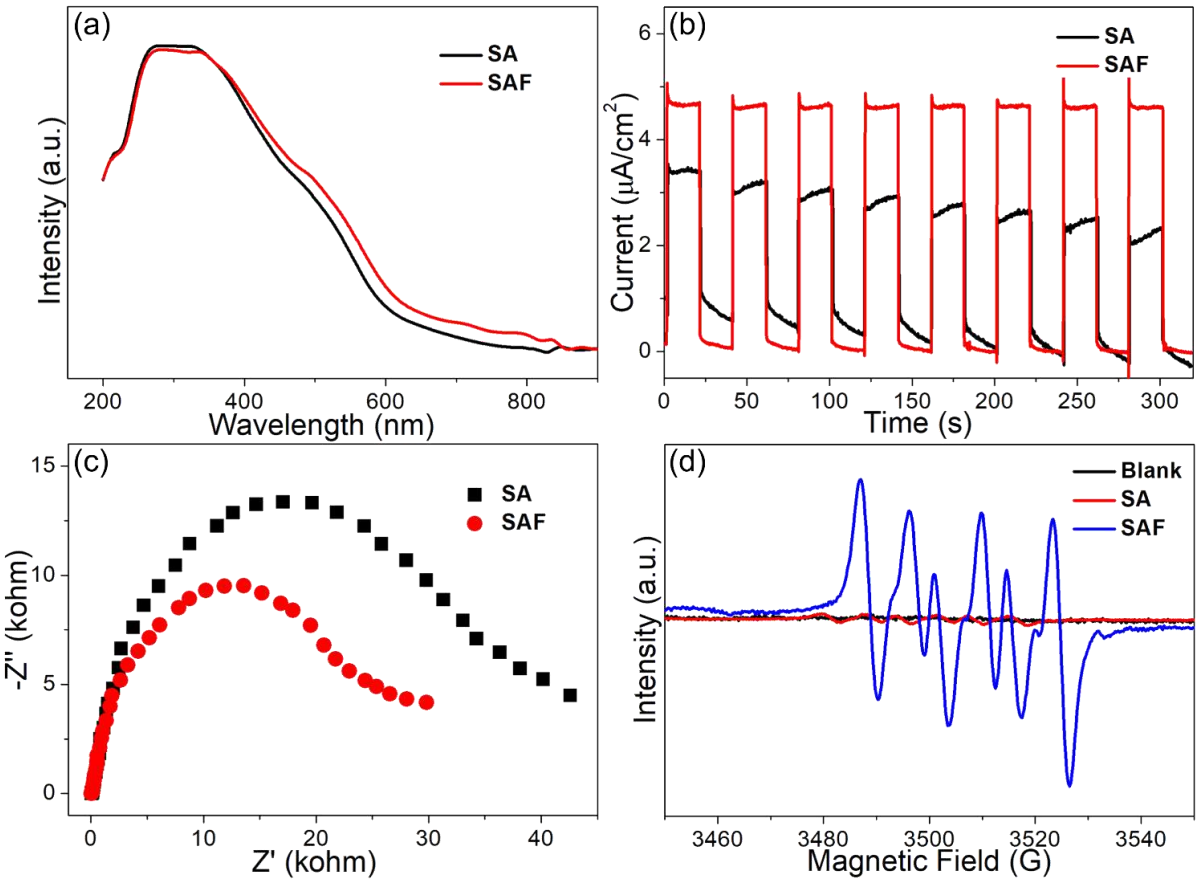


Fig. 6 Comparison of SA and SAF: (a) ultraviolet–visible diffuse reflectance spectra; (b) transient photocurrent; (c) electrochemical impedance spectra; and (d) DMPO-assisted EPR spectra, including a blank

3.3 Aqueous chromium attenuation

Figure 7a compares SA and SAF at an initial pH of 7 with acidified SAF at an initial pH of 3. The blank exhibits little change in normalized Cr(VI) concentration over the plotted period. During the dark-contact stage, the material-containing suspensions show a modest concentration decrease. After illumination begins at t = 0, the SAF profile declines more rapidly than the SA profile, with a steeper decline for SAF at pH 3. The profiles support a qualitative comparison of aqueous Cr(VI) attenuation. A value at the plotted baseline does not establish exact 100% conversion without a validated analytical quantification limit.

The ordering of the concentration profiles supports an association between iron modification and faster Cr(VI) attenuation under the compared conditions. It does not establish a precisely twofold rate enhancement. Figure 7b presents logarithmic concentration plots normalized to the pre-dark concentration. These plots combine dark uptake with concentration changes under illumination, and do not include regression statistics or replicate uncertainty. A rate constant for the illuminated stage requires normalization to the concentration at the onset of irradiation and a defined fitting interval.

SAF preparation includes both solvothermal processing and a subsequent calcination step. These treatments may alter the gangue-derived support as well as the introduced iron species. A matched material subjected to the same processing without the iron precursor is needed to distinguish the contribution of iron from changes caused by solvent exposure and thermal treatment.

The faster concentration decline for SAF at pH 3 is consistent with a pH-dependent response. Acidification can affect chromium oxyanion speciation, surface protonation, and the thermodynamic driving force for reduction, but the present data do not resolve these contributions. Loss of Cr(VI) from the filtrate can reflect adsorption, reduction, or both (Priyadharshini et al., 2025; L. Wang et al., 2024). Demonstrating reduction to Cr(III) and removal of total chromium requires matched speciation measurements and a mass balance that includes the recovered solid.

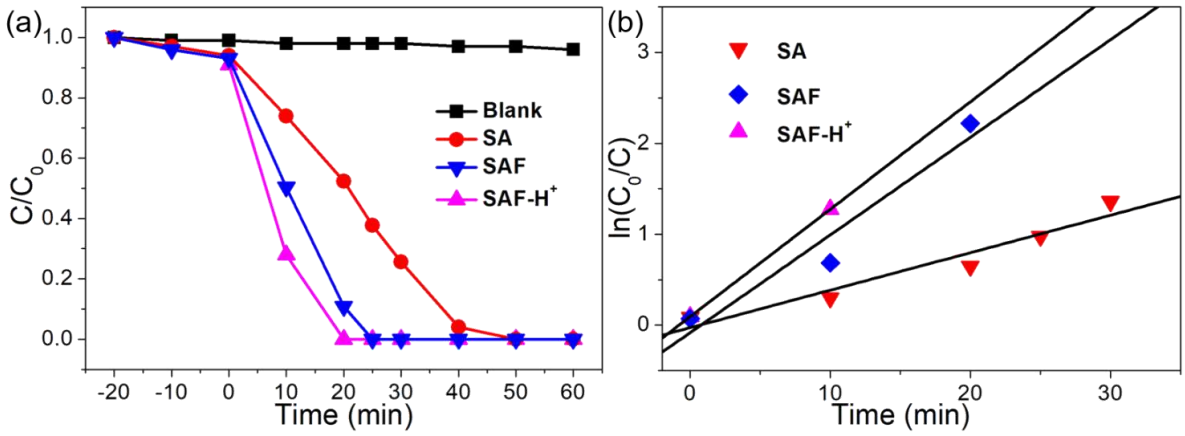


Fig. 7 Aqueous Cr(VI) concentration profiles and kinetic representation: (a) blank, SA and SAF at pH 7, and acidified SAF (SAF–H^+) at pH 3, with the dark stage from −20 to 0 min; (b) logarithmic concentration plots for the material-containing experiments

3.4 Repeated use and post reaction characterization

Five consecutive reaction cycles are shown for SA and SAF in Fig. 8a and b. Both materials retain substantial Cr(VI) attenuation over the displayed cycles. These profiles support qualitative reuse potential, although an exact retained efficiency cannot be established from the displayed endpoints alone. The PXRD traces in Fig. 8c include SA before reaction and SA and SAF after reaction. The main SA reflections persist after use. Because the panel does not include a separate pre-reaction SAF trace, it cannot independently demonstrate unchanged SAF crystallinity. Retention of bulk diffraction features would also not exclude dissolution of a minor iron component.

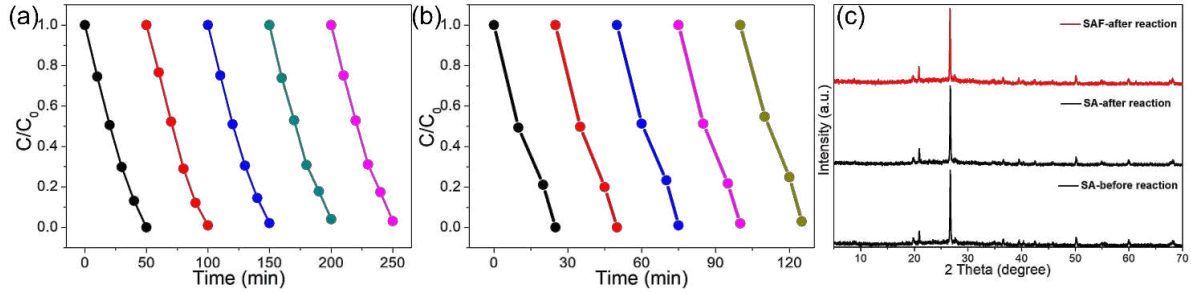


Fig. 8 Repeated reaction cycles under white LED irradiation for (a) SA and (b) SAF; (c) PXRD patterns of SA before reaction, SA after reaction, and SAF after reaction

3.5 Possible pathways and environmental significance

TEMPO, BQ, and IPA strongly suppress Cr(VI) attenuation at the tested endpoint (Table S1). These additives can alter electron transfer, surface interactions, and solution chemistry in addition to intercepting particular reactive species. The inhibition patterns therefore show that the reaction is sensitive to the additives, but they do not uniquely identify electrons, holes, or a single radical as the rate-determining species. In particular, suppression by IPA does not by itself demonstrate that photogenerated holes reduce Cr(VI).

A plausible working interpretation is that light-responsive sites in the gangue-derived material and its iron-containing surface species supply electrons for aqueous Cr(VI) reduction. In acidic solution, the dichromate reduction half-reaction can be written as Eq. 1. Oxygen reduction may compete for electrons and may generate detectable spin-trapped species, but the relative contribution of any oxygen-mediated pathway is unresolved (Djellabi et al., 2022). Charge balance also requires an

oxidation counterpart; the available measurements do not identify the electron donor or establish sustained catalytic turnover.

$$Cr_2O_7^{2-} + 14H^+ + 6e- \rightarrow 2Cr^{3+} + 7H_2O \quad (1)$$

Iron redox cycling could contribute if Fe(II) is generated during illumination, because Fe(II) can reduce Cr(VI). That possibility differs from claiming that Fe(III) itself donates electrons simply because its formal oxidation state is lower than +6. Dissolved iron-mediated chemistry and non-photochemical reduction by residual gangue constituents also remain possible. Distinguishing these pathways requires extended dark controls (Mosisa et al., 2024), dissolved-iron speciation, leachate-only tests, and chromium mass balance.

The environmental relevance is the possibility of converting a mining residue into a reactive water-treatment material while evaluating the incremental effect of iron modification. The present data do not establish treatment of authentic mine water or selectivity in the presence of co-contaminants. Before process application, representative pH and ion matrices, dissolved organic matter, residual total chromium, and iron release should be evaluated. The 800 °C pretreatment, subsequent 600 °C calcination, acid washing, and DMF-based processing also carry material and energy demands; waste origin alone does not demonstrate low cost or environmental benefit. Comparisons with previous gangue-based systems should therefore use matched conditions and include residual concentrations and resource demand, rather than percentage removal alone (Li & Wang, 2018; Zhao et al., 2020; Yang et al., 2025).

4 Conclusions

Iron modification of a calcined and acid-washed gangue-derived material is associated with faster aqueous Cr(VI) attenuation in the presented white-LED concentration profiles. SAF was obtained by solvothermal treatment followed by calcination in air. Surface iron detection, the larger photocurrent response, and the smaller impedance arc are consistent with modification of the material response. The evidence supports further investigation of iron-modified gangue for chromium treatment, while leaving quantitative rate enhancement, the iron phase, electron-transfer pathway, chromium mass

balance, and long-term leaching behavior unresolved. Verification in authentic wastewater and assessment of preparation inputs are needed before practical or sustainability claims can be made.

Statements and Declarations

Funding

This work was supported by the project Comprehensive Evaluation of the Oil-Rich Coal Resource Potential and Utilization Prospects in the Taige Temple Mining Area (No. 6000240419).

Competing interests

The authors declare no competing interests.

Data availability

The data supporting the findings of this study are available from the corresponding author on reasonable request.

Supplementary Information

Supplementary Information contains additional elemental maps of SA and the additive experiment results in Fig. S1 and Table S1.

References

Baruah, P. M., & Singh, G. (2024). Assessing the utilization potential of pumped-out minewater for potability in the water-stressed coal mining region of Jharia, India: A quantitative, qualitative and probabilistic health risk assessment. *Environment, Development and Sustainability*, 26, 6517–6542. https://doi.org/10.1007/s10668-023-02973-z

Bian, Z., Feng, Y., Li, H., & Zhan, J. (2020). Fabrication of Ag3PO4/TiO2@molecular sieve (MS) ternary composites with remarkably enhanced visible light-responded photocatalytic activity and mechanism insight. *Environmental Research*, 190, 109984. https://doi.org/10.1016/j.envres.2020.109984

Biesinger, M. C., Payne, B. P., Grosvenor, A. P., Lau, L. W. M., Gerson, A. R., & Smart, R. St. C. (2011). Resolving surface chemical states in XPS analysis of first row transition metals, oxides and hydroxides: Cr, Mn, Fe, Co and Ni. *Applied Surface Science*, 257, 2717–2730. https://doi.org/10.1016/j.apsusc.2010.10.051

Djellabi, R., Su, P., Elimian, E. A., Poliukhova, V., Nouacer, S., Abdelhafeez, I. A., Abderrahim, N., Aboagye, D., Andhalkar, V. V., Nabgan, W., Rtimi, S., & Contreras, S. (2022). Advances in photocatalytic reduction of hexavalent chromium: From fundamental concepts to materials design and technology challenges. *Journal of Water Process Engineering*, 50, 103301. https://doi.org/10.1016/j.jwpe.2022.103301

Fendorf, S. E. (1995). Surface reactions of chromium in soils and waters. *Geoderma*, 67(1–2), 55–71. https://doi.org/10.1016/0016-7061(94)00062-F

Ge, S., Gu, J., Ai, W., & Dong, X. (2021). Biotreatment of pyrene and Cr(VI) combined water pollution by mixed bacteria. *Scientific Reports*, 11, 114. https://doi.org/10.1038/s41598-020-80053-2

Gupta, S., Vatti, S. K., Gu, Q., Wagh, D., Manyar, H., & Selvam, P. (2023). Defect-induced ordered mesoporous titania molecular sieves: A unique and highly efficient hetero-phase photocatalyst for solar hydrogen generation. *ChemNanoMat*, 9(12), e202300319. https://doi.org/10.1002/cnma.202300319

Islam, S., Mukherjee, S., Sarkar, O., Kamila, S., & Chattopadhyay, A. (2025). Prolonged low-dose chromium (VI) exposure induces oxidative stress, apoptotic genes and epigenetic modification of DNA repair genes in the brain and kidney of Swiss albino mice. *Journal of Applied Toxicology*, 45(7), 1243–1257. https://doi.org/10.1002/jat.4769

Li, S., You, C., Xue, Q., Zhao, Y., Yang, F., Liu, Y., Bai, L., Zhang, M., & Zhuang, C. (2025). Carbon quantum dots and interfacial chemical bond synergistically modulated S-scheme Mn0.5Cd0.5S/BiOBr photocatalyst for efficient water purification. *Journal of Materials Science & Technology*, 214, 255–265. https://doi.org/10.1016/j.jmst.2024.07.015

Li, Y., & Wang, X. (2018). Chromium (VI) reduction in aqueous solutions using coal gangue. *Desalination and Water Treatment*, 113, 102–108. https://doi.org/10.5004/dwt.2018.22293

Liu, D., Liu, X., Guo, Z., Li, Q., Yang, J., Xing, H., & Chen, D. (2023). Aluminum-porphyrin metal–organic frameworks for visible-light photocatalytic and sonophotocatalytic Cr(VI) reduction. *Inorganic Chemistry*, 62(48), 19812–19820. https://doi.org/10.1021/acs.inorgchem.3c03563

Liu, H., Li, P., Fang, Y., Hu, X., & Chen, Q. (2025). Correlation between ligand-mediated silver species on TiO2 nanosheet with the photocatalytic hydrogen evolution activities. *Journal of Colloid and Interface Science*, 683, 773–785. https://doi.org/10.1016/j.jcis.2024.12.124

Liu, W., Guo, Z., Jin, Z., Chen, D., Lu, T., Jia, P., & Xing, H. (2022). Visible-light-driven sonophotocatalysis for enhanced Cr(VI) reduction over mixed-linker zirconium-porphyrin MOFs. *Catalysis Science & Technology*, 12, 2176–2183. https://doi.org/10.1039/D1CY02346B

Lv, S., Zuo, J., Zhang, S., Liang, S., Wang, J., & Wei, D. (2023). L-Arginine modified lignin composite carbon quantum dots fluorescent probe for Cr(VI) detection. *Macromolecular Chemistry and Physics*, 224(4), 2200380. https://doi.org/10.1002/macp.202200380

Mosisa, M. T., Zhang, P., Su, Z., Wu, B., Chen, L., Liao, Y., Farooq, A., Lu, D., Abdeta, A. B., Kuo, D.-H., Lin, J., & Chen, X. (2024). A novel V/S co-doped BiOBr catalyst for high-efficiency catalytic reduction of toxic organic and hexavalent chromium pollutants under dark. *Journal of Environmental Chemical Engineering*, 12(2), 112111. https://doi.org/10.1016/j.jece.2024.112111

Nizam, A., Warrier, V. G., Devasia, J., & Ganganagappa, N. (2022). Magnetic iron oxide nanoparticles immobilized on microporous molecular sieves as efficient porous catalyst for photodegradation, transesterification and esterification reactions. *Journal of Porous Materials*, 29, 119–129. https://doi.org/10.1007/s10934-021-01150-9

Priyadharshini, R., Elanchezhiyan, S. SD., Prabhu, S. M., & Meenakshi, S. (2025). Bimetallic oxide integrated chitosan matrix for adsorption coupled reduction of Cr(VI) from aqueous solution. *Separation and Purification Technology*, 370, 133158. https://doi.org/10.1016/j.seppur.2025.133158

Rajappa, V., Mohan, S., Bharathkumar, S., Rokhum, S. L., Fatehmulla, A., Valdes, H., & Ilangovan, R. (2024). Fe, N dual-doped cerium oxide photocatalyst manifesting the simultaneous degradation of dye–heavy metal mixed pollutants under sunlight. *Industrial & Engineering Chemistry Research*, 63(50), 21760–21770. https://doi.org/10.1021/acs.iecr.4c03013

Ren, X., Xu, M., Ma, L., Yan, X., Zhang, Y., Dai, T., & Xu, J. (2026). Hydrothermal preparation of coal gangue-derived heterogeneous structures for selective adsorption enhanced photocatalytic removal of Cr(VI) ions in tar-rich coal mine water. *Scientific Reports*, 16, 1730. https://doi.org/10.1038/s41598-025-31321-6

Sun, X.-Z., Yi, X.-H., Li, Y.-H., Wang, C.-C., & Wang, P. (2023). Organic superconductor modified NH2-UiO-66 for boosting photocatalytic Cr(VI) elimination under low-power ultraviolet light. *New Journal of Chemistry*, 47(37), 17517–17524. https://doi.org/10.1039/D3NJ03248E

Sun, Y., Szulejko, J. E., Kim, K.-H., Kumar, V., & Li, X. (2023). Recent advances in the development of bismuth-based materials for the photocatalytic reduction of hexavalent chromium in water. *Chinese Journal of Catalysis*, 55, 20–43. https://doi.org/10.1016/S1872-2067(23)64553-X

Sutrisna, P. D., Kurnia, K. A., Siagian, U. W. R., Ismadji, S., & Wenten, I. G. (2022). Membrane fouling and fouling mitigation in oil–water separation: A review. *Journal of Environmental Chemical Engineering*, 10(3), 107532. https://doi.org/10.1016/j.jece.2022.107532

Wang, D., Wu, D., Wei, A., Gao, J., Pan, C., Mao, Z., & Feng, Q. (2025). Scalable, high flux of electrospun nanofibers membrane for rapid adsorption-reduction synergistic removal of Cr(VI) ions in wastewater. *Separation and Purification Technology*, 360, 130747. https://doi.org/10.1016/j.seppur.2024.130747

Wang, L., Ren, Y., Zhao, H., Li, H., Niu, X., Zhang, D., Fan, H., & Wang, K. (2024). Synergistic purification of chromium-containing wastewater via adsorption-photocatalysis induced by multiple defect-containing CuS/Cv-CNNs. *New Journal of Chemistry*, 48, 4507–4520. https://doi.org/10.1039/D3NJ05767D

Wang, R.-Q., Chen, W.-P., Zhang, Y.-R., Song, K., Tian, Y., Li, J.-X., Shi, G.-F., & Wang, G.-Y. (2023). Development and study of a bifunctional photocatalyst based on SAPO-34 molecular sieve. *New Journal of Chemistry*, 47(14), 6563–6576. https://doi.org/10.1039/D3NJ00087G

Wu, M., Zhang, M., Shen, L., Wang, X., Ying, D., Lin, H., Li, R., Xu, Y., & Hong, H. (2023). High propensity of membrane fouling and the underlying mechanisms in a membrane bioreactor during occurrence of sludge bulking. *Water Research*, 229, 119456. https://doi.org/10.1016/j.watres.2022.119456

Xu, X., Xie, J., Li, Y., Wu, S., Yang, X., Eltzov, E., & Jia, K. (2025). Carboxylated polyarylene ether nitrile modified polysulfone membrane with enhanced anti-fouling for oily water separation and hexavalent chromium removal. *Separation and Purification Technology*, 364, 132486. https://doi.org/10.1016/j.seppur.2025.132486

Yang, J., He, L., Zhao, S., Shi, Y., & Dusu, W. (2025). Research progress of coal gangue-based modified materials and the sewage treatment field. *Sustainable Energy & Fuels*, 9, 6027–6049. https://doi.org/10.1039/D5SE00868A

Zhao, R., Zhang, X., Su, Y., Liu, Z., & Du, C. (2020). Unprecedented catalytic activity of coal gangue toward environmental remediation: Key role of hydroxyl groups. *Chemical Engineering Journal*, 380, 122432. https://doi.org/10.1016/j.cej.2019.122432

Zhao, Z., An, H., Lin, J., Feng, M., Murugadoss, V., Ding, T., Liu, H., Shao, Q., Mai, X., Wang, N., Gu, H., Angaiah, S., & Guo, Z. (2019). Progress on the photocatalytic reduction removal of chromium contamination. *The Chemical Record*, 19(5), 873–882. https://doi.org/10.1002/tcr.201800153

Zheng, J., Sun, L., Xue, Y., Ye, L., & Fan, Q. (2024). Construction of pillared-layer metal–organic frameworks as an all-visible-light switchable photocatalyst for aqueous Cr(VI) reduction. *Inorganic Chemistry*, 63(34), 15841–15850. https://doi.org/10.1021/acs.inorgchem.4c01946

Zhu, B., Jiang, C., Xu, J., Zhang, Z., Fu, J., & Yu, J. (2025). Quantum dots in S-scheme photocatalysts. *Materials Today*, 82, 251–273. https://doi.org/10.1016/j.mattod.2024.11.012

Supplementary Files

This is a list of supplementary files associated with this preprint. Click to download.

- SupportingInformation.docx